ADVANCING EARTH AND SPACE SCIENCE

JGR Space Physics

RESEARCH ARTICLE
10.1029/2022JA030929

Key Points:

- We propose a causal link between mid-latitude sporadic E-layer structuring and turning shears in the neutral flow
- Ekman-type instabilities have been connected to mesosphere and lower thermosphere (MLT) dynamics. Here, they are further connected to quasi-periodic echoes
- Coherent scatter radar imagery of structured sporadic E layers is suggestive of Ekman-type instability in the MLT

Supporting Information:

Supporting Information may be found in the online version of this article.

Correspondence to:

M. X. Bui,
mb2374@cornell.edu

Citation:

Bui, M. X., Hysell, D. L., & Larsen, M. F. (2023). Midlatitude sporadic E-layer horizontal structuring modulated by neutral instability and mixing in the lower thermosphere. *Journal of Geophysical Research: Space Physics*, *128*, e2022JA030929. https://doi.org/10.1029/2022JA030929

Received 15 AUG 2022
Accepted 17 JAN 2023

Midlatitude Sporadic E-Layer Horizontal Structuring Modulated by Neutral Instability and Mixing in the Lower Thermosphere

Michelle X. Bui[1], David L. Hysell[1], and Miguel F. Larsen[2]

[1]Department of Earth and Atmospheric Sciences, Cornell University, Ithaca, NW, USA, [2]Department of Physics and Astronomy, Clemson University, Clemson, SC, USA

Abstract Observations of 30-MHz coherent backscatter from sporadic-*E* ionization layers were obtained with a VHF imaging radar located in Ithaca, New York. The volume probed by the radar lies at relatively high magnetic latitudes, on the northern edge of the mid-latitude region and underneath the ionospheric trough. Banded, quasi-periodic (QP) echoes observed from Ithaca are similar to those found in lower midlatitude regions. The Doppler shifts observed are smaller and, so far, do not appear to reach the threshold for Farley-Buneman instability. However, many of the echoes exhibit fine-scale structure, with secondary bands or braids oriented obliquely to the primary bands. Secondary bands have been seen only rarely at lower middle latitudes. In previous observations, the QP scattering has been linked to unstable neutral wind shears. Neutral wind shear commonly found in the lower thermosphere could play a key role in the formation of these irregularities and explain some morphological features of the resulting plasma density irregularities and the radar echoes. We consider whether neutral instability and turbulence in the lower thermosphere is the likely cause for some of the structuring in the sporadic- *E* layers. Results of 3D numerical simulations of atmospheric dynamics in the mesosphere to lower thermosphere support the proposition. In particular, we focus on Ekman-type instabilities that, like the more common Kelvin-Helmholtz instabilities, are inflection point instabilities, although specifically associated with turning shears, and result in convective rolls aligned close to the mean wind direction, with smaller-scale secondary waves aligned normal to the primary structures.

1. Introduction

The transition region from the mesosphere to the lower thermosphere is characterized by a change in the static stability from the less stable upper mesosphere to the increasing static stability in the mesopause and lower thermosphere. The same altitude range encompasses the transition from enhanced turbulent diffusion to dominant molecular diffusion that occurs at the turbopause. In the same region, there are ubiquitous strong winds and turning shears generally attributable to the tides but enhanced by the tendency for small scale processes, such as gravity waves, to break there and deposit momentum that accelerates the flow. The article by Liu (2017) gives an overview of the dynamics of the region and provides references to earlier related work.

Kelvin-Helmholtz shear instabilities have been a focus of a large number of studies of the dynamics of mesosphere and lower thermosphere (MLT) region since the shears frequently are strong enough to meet the necessary Richardson number criterion for that type of instability, that is, $Ri < 1/4$. However, the speed and turning shears that occur there are conducive to other neutral instabilities as well. Larsen et al. (2004) and Hurd et al. (2009) pointed out the similarities between the atmospheric boundary layer and the MLT transition region and presented lidar observations that were consistent with the expected characteristics for convective rolls associated with Ekman-type inflection point instability. Observations from the MLT region are extremely limited in general in spite of the critical importance of the region. Sporadic- *E* layers occur in the MLT transition region, and the plasma irregularity structure associated with the layers can be observed with coherent scatter radars. In a series of papers, we have used such observations to analyze both the electrodynamics responsible for the plasma irregularities and the neutral shear instabilities and upwelling that drive the processes. The recent paper by Hysell and Larsen (2021) discusses coherent scatter data showing evidence for neutral shear instabilities of the Kelvin-Helmholtz type and the evolution of secondary instabilities. References to earlier work can also be found in that article.

10.1029/2022JA030929

In this article, we report on observations of 30-MHz coherent backscatter from patchy sporadic- *E* ionization layers (E_s layers) obtained using a radar in Ithaca, New York, in the summer of 2021. This is a follow-on to the preliminary study presented by Hysell and Larsen (2021). The data set considered here is more extensive and includes 13 events observed between July and September 2021. The current study was also supported by the Millstone Hill incoherent scatter radar near Bedford, MA, and a new coherent scatter radar located in Clemson, SC, although we focus here on the Ithaca observations. The work presented here represents the latest in a series of E_s-layer observations that began in Clemson in the 1990s and continued in the sub-tropics from 2002 to 2016 (e.g., Hysell et al., 2018 and references therein).

The new observations differ from earlier ones in that they represent the high-latitude boundary of the mid-latitude region, adjoining the subauroral zone and beneath the mid-latitude trough. Despite this and the fact that the observations were made during deep solar minimum, we found a high rate of occurrence of E_s-layer irregularities and quasiperiodic (QP) echoes. In the summer of 2021, we observed more QP-echo activity over the Great Lakes region (with the radar in Ithaca) than over the South Atlantic region (with the radar in Clemson). This and the distinct morphology of the echoes seen from Ithaca prompt an investigation into new physics that may be unique to the region. As in the sub-tropics, echoes observed from Ithaca often take the form of long bands aligned northwest to southeast and propagating to the southwest. Bands tend to occur in clusters separated by intervals of 40–60 min. There can be considerable fine structure in the bands. Unlike the sub-tropics, the Doppler shifts of the echoes observed from Ithaca tend to be relatively small (≤100 m/s) and have yet to be seen approaching the presumptive ion acoustic speed and the threshold for Farley-Buneman instability (approximately 300 m/s for iron ion layers). However, the echoes seen with the Ithaca radar frequently exhibit secondary bands or braids oriented at oblique angles to the primary bands and with smaller wavelengths. Secondary features have been seen only rarely at lower middle latitudes (e.g., Hysell et al., 2012). They could signify another type of primary instability or a secondary instability emerging from the primary.

In this paper, we investigate the morphology of the E_s-layer echoes observed with the Ithaca radar. The analysis will focus mainly on neutral atmospheric dynamics in the MLT region. Neutral instabilities believed to predominate in the mesosphere and lower thermosphere could explain several gross features of the radar echoes and underlying E_s-layer structuring, due to the importance of surrounding collisional effects. The echoes then become a way to diagnose neutral dynamics and instabilities in a region of space otherwise difficult to probe.

2. Background

Reflections from sporadic ionization layers in the mid-latitude *E* region were among some of the earliest ionospheric effects detected by radio (see e.g., Layzer, 1969; Whitehead, 1972, 1989 for reviews). The discovery that patchy sporadic- *E* layers could also be the source of coherent radar backscatter renewed interest in the layers and the plasma density irregularities within (Riggin et al., 1986). Observations of striking, quasiperiodic (QP) bands of backscatter from the Middle and Upper Atmosphere (MU) radar in Japan spurred considerable interest and research (Yamamoto et al., 1991, 1992), culminating in a series of dedicated sounding rocket experiments focusing on background neutral and plasma state parameter measurements near the layers (e.g., Fukao et al., 1998; Larsen et al., 1998). Subsequent experimental programs aimed at investigating coherent scatter from E_s layers and attendant phenomena have taken place around the world (e.g., Chu and Wang, 1997; Hysell & Burcham, 1999; Larsen et al., 2007; Rao et al., 2008; Woodman et al., 1999).

Several causal mechanisms rooted in plasma instabilities were proposed following the initial MU Radar QP-echo observations (Cosgrove & Tsunoda, 2002, 2004; Hysell et al., 2002b; Seyler et al., 2004). The issue regarding which plasma processes dominate remains unresolved, although it is important to consider that coherent scatter generally does not accompany blanketing layers, implying an essential role for intermediate-scale layer structuring. The resemblance of certain aspects of the QP echoes to billows and rolls seen in sporadic- *E* ionization layers earlier at the Arecibo Observatory (see Miller and Smith, 1978; Smith and Miller, 1980) together with evidence of highly structured neutral winds in the vicinity of the layers prompted an investigation of the causal role of neutral atmospheric dynamics and instability (Larsen, 2000). More recent findings arguing that the MLT region is very often dynamically unstable and possibly even convectively unstable reinforce the connections between structured E_s layers, QP echoes, and neutral atmospheric dynamics and instability (e.g., Hecht et al. (2004)).

Although much of the aforementioned research focused on planar wind shear and Kelvin Helmholtz (KH) instability, Larsen et al. (2004) pointed out that this is only a special case of more general turning shears and inflection point instabilities. Hysell et al. (2012) estimated MLT wind profiles in the vicinity of patchy E_s layers giving rise to QP echoes at the Arecibo Radio Observatory, finding turning shears that were dynamically unstable with fast-growing eigenmodes that matched the E_s-layer structuring in terms of scale size and propagation speed and direction.

Larsen et al. (2004) furthermore made the connection between the neutral winds in the MLT, which exhibit turning shears and a general increase in amplitudes above the mesopause, with the atmospheric boundary layer, a region known to exhibit a variety of instabilities including Ekman-type instabilities. While the causes of the flows in the MLT and the atmospheric boundary layer are very different, the flows themselves can be similar, and the similarity invites an investigation of the instabilities that may result and the possible connections to emergent phenonema in E_s layers. The coherent scatter radar data presented in this paper provide a means of probing these connections further.

3. Data Presentation

We present observations from a 30-MHz coherent scatter imaging radar deployed near Ithaca, New York (42.444°N, 76.502°W, 51.64°N geomagnetic). The main beam of the radar is directed toward the northwest and illuminates targets in the *E* region above the Great Lakes at ranges mainly between 200 and 400 km. The radar nominally uses an interpulse period of 4 ms (600 km), permitting the unambiguous detection of Doppler shifts between ±625 m/s. For these observations, we employed a 28-bit maximal length binary phase code with a bit width of 10 μs and a duty cycle of 7%. The transmitter peak power is 8 kW.

The antenna array employs 16 five-element Yagi antennas arranged strategically into six groups. Transmission is on two antenna groups which together constitute a uniform linear array of eight antennas with a half-power full beamwidth of approximately 10°. Reception is on all six groups of antennas spaced strategically in a plane from which six data streams can be processed independently, giving 15 nonredundant baselines for interferometry. The longest interferometry baseline is approximately 15 wavelengths. The radar itself uses software-defined signal synthesis and reception. Additional system hardware and software details and some preliminary observations were presented by Hysell and Larsen (2021).

Supporting instrumentation includes the Digisonde at Alpena, Michigan (see http://spase.info/VWO/Numerical-Data/GIRO/CHARS.PT15M). While the Alpena Digisonde does not probe a common volume with the radar in Ithaca, sporadic- *E* layer activity over Alpena was highly correlated with coherent scatter detected from Ithaca in 2020 and 2021. Other complementary instrumentation includes the incoherent scatter radar (ISR) at the Millstone Hill Observatory (MHO) outside Bedford, Massachusetts. The Millstone ISR can observe state parameters in the *F* region sharing common magnetic field lines with the *E*-region volume probed by the coherent scatter radar in Ithaca. Two campaigns with MHO support were conducted in the summer of 2021 to look for evidence of coupled *E*- and *F*-region instabilities, irregularities, and processes.

In 2021, a second 30-MHz coherent scatter radar with characteristics very similar to the Ithaca radar was deployed near Clemson, South Carolina (34.628°N, 82.826°W, 43.60°N geomagnetic). The Clemson radar can probe backscatter from FAIs in the *E* region immediately to the north. Moreover, it can also probe FAIs in the *F* region visible to MHO and on magnetic field lines passing through the *E* region volume observed by the Ithaca radar over the Great Lakes (e.g., Swartz et al. (2000)).

We present no results from Millstone Hill or the Clemson radar in this study except to note that no evidence was found of *F*-region ionospheric irregularities over the Great Lakes region during the campaigns. In other words, the observations do not support at this time the conjecture that the QP echoes observed from Ithaca are part of a coupled system of *E*- and *F*-region irregularities and instabilities. Our campaign studies have been limited to a few days of common-volume observations, however, and more extensive studies are required to establish the point.

The most reliable telltales of sporadic- *E* activity in the Great Lakes region arguably came from autonomous, real-time reports of amateur radio communications in the 6-m band (see http://www.dxmaps.com). This information is telltale mainly of reflection rather than scattering and so represents more of a necessary than a sufficient condition for QP echoes. Nonetheless, community-sourced data such as these are valuable in geographic regions which are otherwise sparsely instrumented.

10.1029/2022JA030929

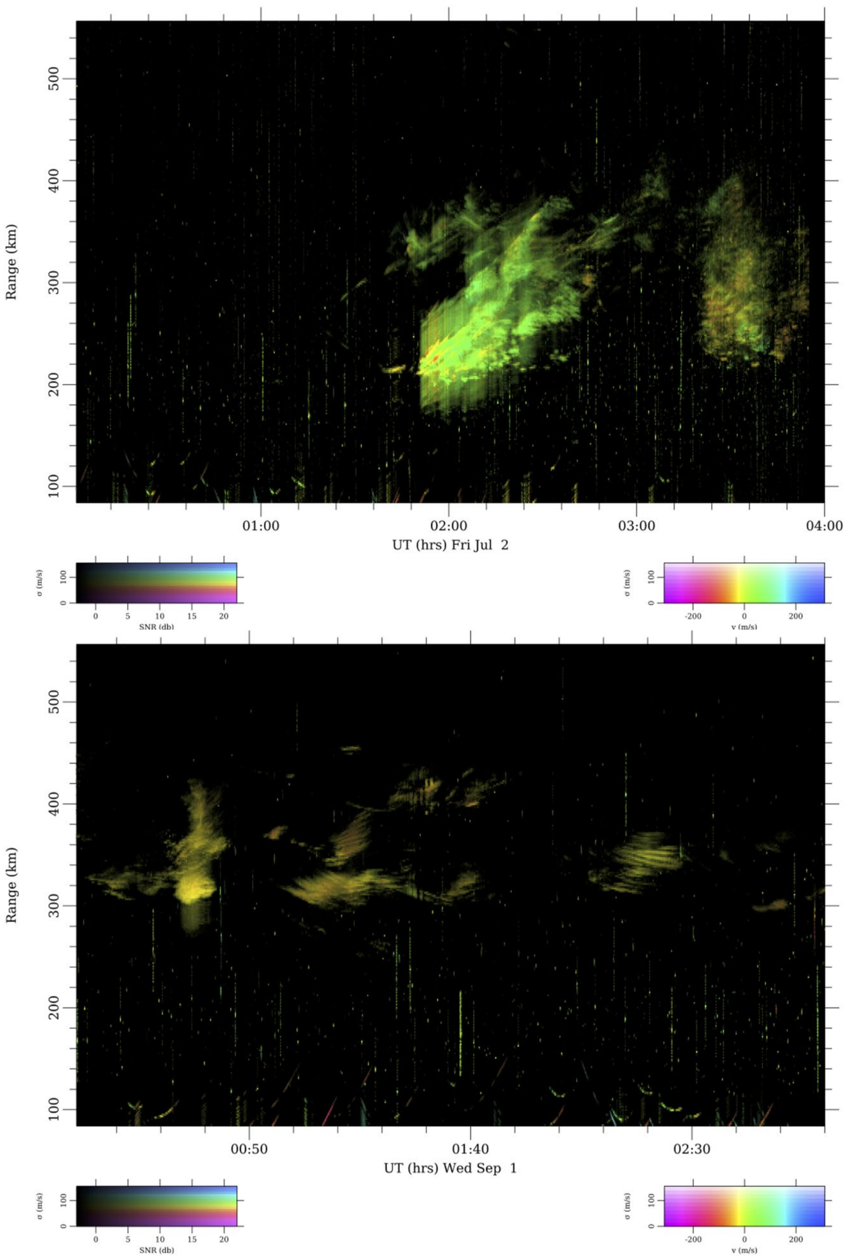

Figure 1. Range-Time-Doppler-Intensity (RTI) plot for (a) 2 July and (b) 1 September 2021 between 0:00 and 4:00 UT. The pixel brightness, hue, and saturation reflect the signal-to-noise ratio, Doppler shift, and spectral width, respectively, according to the legends shown. The RTI plots contain many specular and non-specular meteor echoes in addition to echoes from E_s-layer irregularities.

Figure 1 shows backscatter of sporadic- *E* structures seen by the Ithaca radar between 0:00 and 4:00 UT on 2 July and 1 September 2021. These events, which are otherwise fairly typical of the entire data set, are highlighted because of the relative absence of fine structure in range in their range-time-intensity (RTI) representations. Both events illustrate the tendency for echoes to occur in patches separated in time by about 30–90 min. Both events exhibit relatively small Doppler shifts with magnitudes less than 100 m/s. Radar imagery (see below) reveals that the echoes come from bands extending from the northwest to the southeast and propagating slowly westward. As the radar line of sight is to the northwest, the corresponding range rates (time rates of change of range) are mainly positive but small. The Doppler shifts are roughly in agreement with the range rates, although there are small discrepancies. The echo strengths are comparable to what has been observed in the sub-tropics using systems with comparable sensitivity.

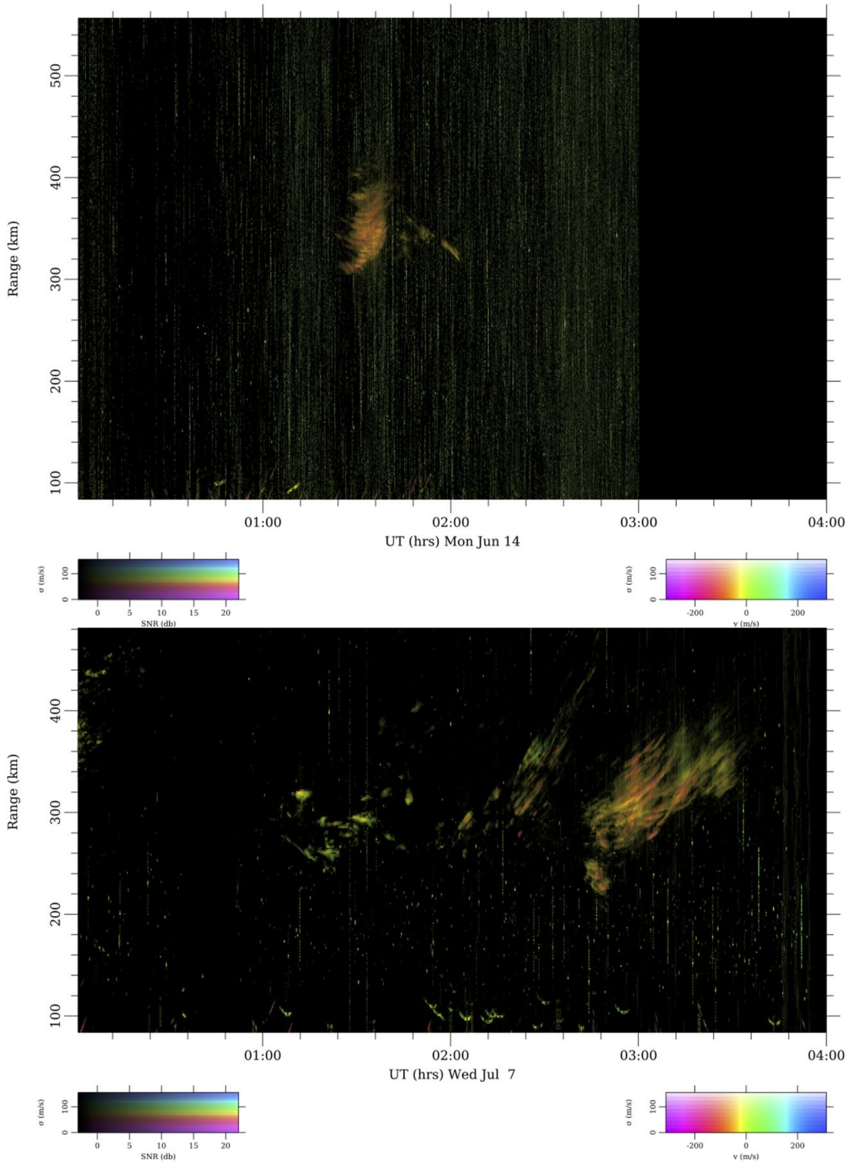

Figure 2. Range-Time-Doppler-Intensity (RTI) plots for (a) 14 June 2021, and (b) 7 July 2021, between 0:00 and 4:00 UT. The legends are the same as in Figure 1.

Backscatter observed between 00:00 and 04:00 UT on 14 June and 7 July 2021, is presented in Figure 2. As with Figure 1, the Doppler shifts here are relatively small (≤100 m/s) but distinctly red shifted at times, and the range rates correspond roughly to the Doppler shifts. These events were selected for the preponderance of fine structure in the RTI plots. This is particularly clear in the red-shifted patches in both events where barely-resolved, closely-spaced streaks are evident throughout the backscatter. Similar fine structure was present in about half the echo patches observed in 2021 and mainly in red-shifted patches.

Aperture-synthesis imaging methods can be applied to data from the Ithaca and Clemson radars to examine within-the-beam structuring of the backscatter. The imaging methodology and its merits and limitations were described in detail by Hysell and Chau (2006). We compute the spatial covariance of the backscattered signal using all available interferometry baselines (the visibilities). A linear transformation can be used to convert visibility to brightness, a description of the backscatter intensity versus bearing (Thompson, 1986). The transformation is underdetermined and is consequently preformed using regularization with Shannon's entropy serving as the regularization metric (Jaynes, 1982; Skilling & Bryan, 1984; T. Y. Yu et al., 2000). Brightness is estimated in every range gate and Doppler bin separately, and the results are combined into three-dimensional images.

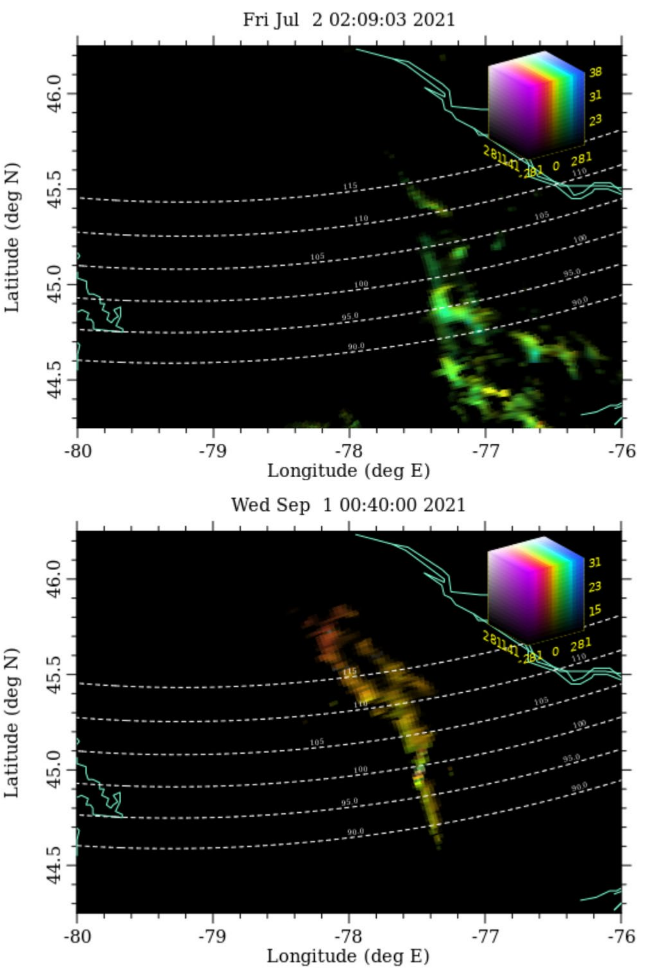

Figure 3. Radar images for (a) 2 July and (b) 1 September 2021 at the UT times indicated. As with the RTI plots, the brightness, hue, and saturation of the image pixels correspond to the intensity, Doppler shift, and spectral width according to the legend shown. The dashed white contours indicate the altitude of the locus of perpendicularity assuming straight-line propagation. In both images, the backscatter is dominated by long, slowly-propagating bands of scatterers separated by about 10–20 km distance.

Two-dimensional plots are obtained by considering only echoes coming from near the locus of perpendicularity for the radar. Error propagation is performed on the basis of error estimators derived by Hysell and Chau (2006). The imaging cadence is nominally once every 3 seconds. Sequential images can be animated to yield insights into echo evolution.

Selected radar images are shown in Figure 3 for the 2 July and 1 September 2021 events corresponding to Figure 1 when relatively little fine structure was evident in the RTI plots. The images give a plan view of the irregularities in the radar-illuminated region. The dashed white lines indicate the altitude where the condition for field-aligned backscatter assuming straight-line propagation is met. In fact, refraction can be expected to allow significant departures from straight-line propagation within the layers (Hysell et al., 2002a), and so the altitudes shown give only rough indications of altitude. Refraction can also distort and conceal structuring which is consequently being rendered approximately.

The main features in both images are banded structures extending from northwest to southeast. Radar images reveal that bands propagate very slowly to the southwest in both cases. The Doppler shifts are small ($\lesssim$100 m/s) in both cases and slightly positive (negative) on July 2 (Sep. 1), in agreement with the apparent motion of the bands relative to the radar line of sight. The features are somewhat irregular and distorted and contort as they propagate. Observations reveal only limited fine structuring.

Figure 4 shows images for 14 June and 7 July 2021 corresponding to the RTI plots in Figure 2 which were selected for their fine structure. The images show bands with significant fine structuring. The primary bands appear to be woven with secondary braids aligned across the primaries. Whereas the bands are propagating very slowly to the southwest, the braiding appears to be propagating northwest at 40–50 m/s in the direction approximately opposite the radar line of sight. The secondary structuring appears to break up after about 10 min in both cases. Similar remarks apply to the highly structured echoes described by Hysell and Larsen (2021).

Finally, Figure 5 shows a RTI plot along with two selected radar images for an event observed on 28 June 2021. The echoes late in the event were characterized by small positive Doppler shifts and exhibited relatively little fine structure. This is borne out in the corresponding radar imagery which features a single, long, primary band propagating slowly to the southwest. Just earlier the event, however, the echoes exhibited more fine structure in their RTI representation and also acquired a distinct red shift. The corresponding images are indicative of a highly structured band with transverse braiding along its length. In animated series of images, the braiding appears to propagate along the band toward the northwest. Both varieties of echoes observed from Ithaca were therefore present in the same event, albeit at slightly different times.

4. Theory and Modeling

Steady, deep, long-lived rolls are frequently observed in the planetary boundary layer under neutral static stability conditions. The cause of instability is the inflection point in the shear that exists in Ekman spiraling flow, which is a solution to the linearized compressible Navier-Stokes equations with a balance between the Coriolis force, pressure gradient force, and viscosity (Ekman, 1905). In studies of boundary-layer dynamics, the Ekman flow is often considered a useful prototype even if the underlying conditions are unrealistic. Note that in these studies, the Reynolds number is interpreted as the turbulent Reynolds number.

The boundary conditions for Ekman flow include a non-slip condition at one vertical boundary and asymptotic relaxation to the geostrophic wind at infinity. Although no such boundary conditions exist in the MLT region where the winds are dominated by the tides, we consider Ekman flow to be a useful prototype here as well since

10.1029/2022JA030929

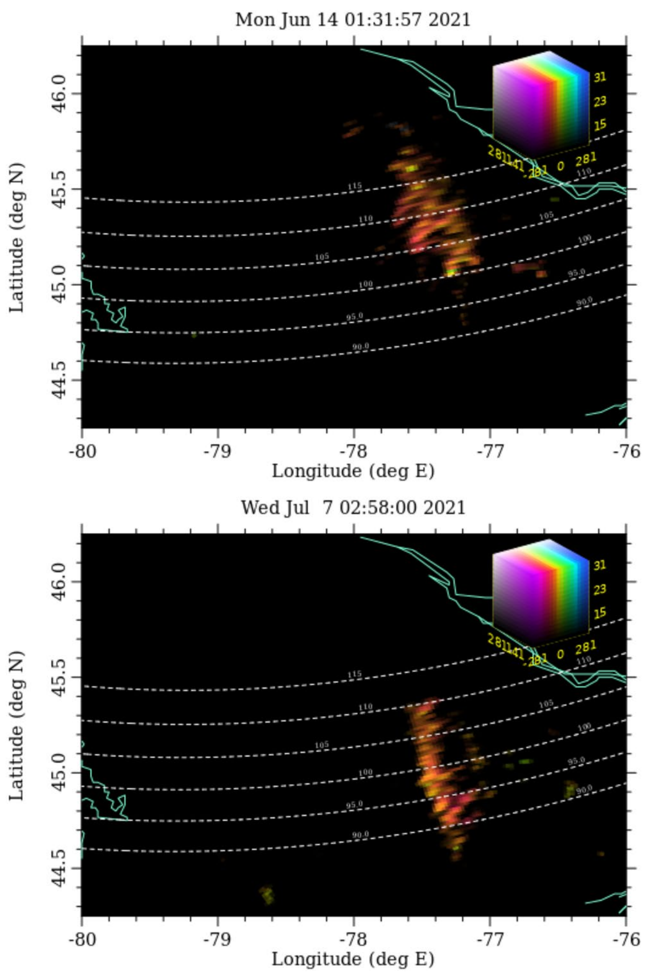

Figure 4. Selected radar images for (a) June 14 and (b) 7 July, 2021, at the UT times shown. Both images feature prominent bands with secondary cross-hatching or braided structure. While the bands propagate to the southwest, the secondary structures propagate to the northwest, along the bands and away from the radar.

the wind measurements generally have a similar spiral altitude variation in many cases, that is, exhibiting small wind speeds below the mesopause and larger winds above asymptoting to their thermospheric limit, and turning shear throughout (Larsen, 2000; Larsen et al., 2004).

Ekman flow was considered by Lilly (1966) and others subsequently who examined the effects of Reynolds number, latitude, and geostrophic wind direction on stability. Analysis methods have included linear eigenvalue analysis as well as direct numerical and large eddy simulations (e.g., Faller and Kaylor (1966); Mason and Sykes (1980); Leibovich and Lele (1985); Coleman et al. (1990)). Characteristics of so-called type-1 and type-2 instabilities especially have received close scrutiny under a number of different flow conditions. The salient features of these instabilities and the distinctive rolls they produce are described below. More extensive details can be found in the references given.

At the poles, above a critical Reynolds number of about 55, type-2 instability characterized by viscous traveling waves emerge with roll axes oriented at about $-20°$ with respect to the asymptotic wind direction. Above a critical Reynolds number of about 113, meanwhile, type-1 instability, an inviscid emerges as an inviscid inflection-point instability characterized by stationary waves oriented at about $7°$ relative to the asymptotic wind direction, emerge. Although type-1 instability has a higher Reynolds number threshold than type 2, it also has a higher growth rate and tends to dominate when it can be excited. It also has a significantly smaller dominant wavelength than type 2.

A third class of instability was later identified by Lingwood (1995). This is an absolute instability in an idealized, homogeneous system, a situation that may not be representative of real conditions in nature.

Ekman flow stability is affected by latitudinal variations and the geostrophic wind direction. At lower Reynolds number, Leibovich and Lele (1985) showed that Ekman flow associated with eastward (westward) geostrophic wind is less (more) unstable at middle latitudes than at the poles. The stability for northward and southward geostrophic winds is unchanged. However, this trend becomes less important as the Reynolds number increases.

Once established, the rolls can saturate to attain an equilibrium state. If the Reynolds number is sufficiently large, however, the rolls become subject to three-dimensional secondary instabilities, aligned obliquely to the primary rolls and drawing free energy from shears both along and across them (Dubos et al., 2007). The growth rate of secondary instability is comparable to that of primary instability, but the dominant wavelength is approximately four times smaller. The growth rate moreover depends on latitude and the geostrophic wind direction. At middle latitudes, eastward (westward) geostrophic winds are relatively destabilizing (stabilizing). At the poles, the direction of the geostrophic wind has little effect on stability.

Here, we attempt to reproduce the main features of an Ekman-type instability under conditions approximately representative of the lower thermosphere. These will be compared with the most salient features in the coherent scatter radar observations.

4.1. Model Equations

To investigate Ekman structures, we consider boundary-layer flow in a three-dimensional semi-infinite Cartesian region (x, y, z) extending in the vertical from approximately the mesopause ($z = 0$) upward. The system of governing equations includes the continuity equation for incompressible flow:

$$u_x + v_y + w_z = 0 \tag{1}$$

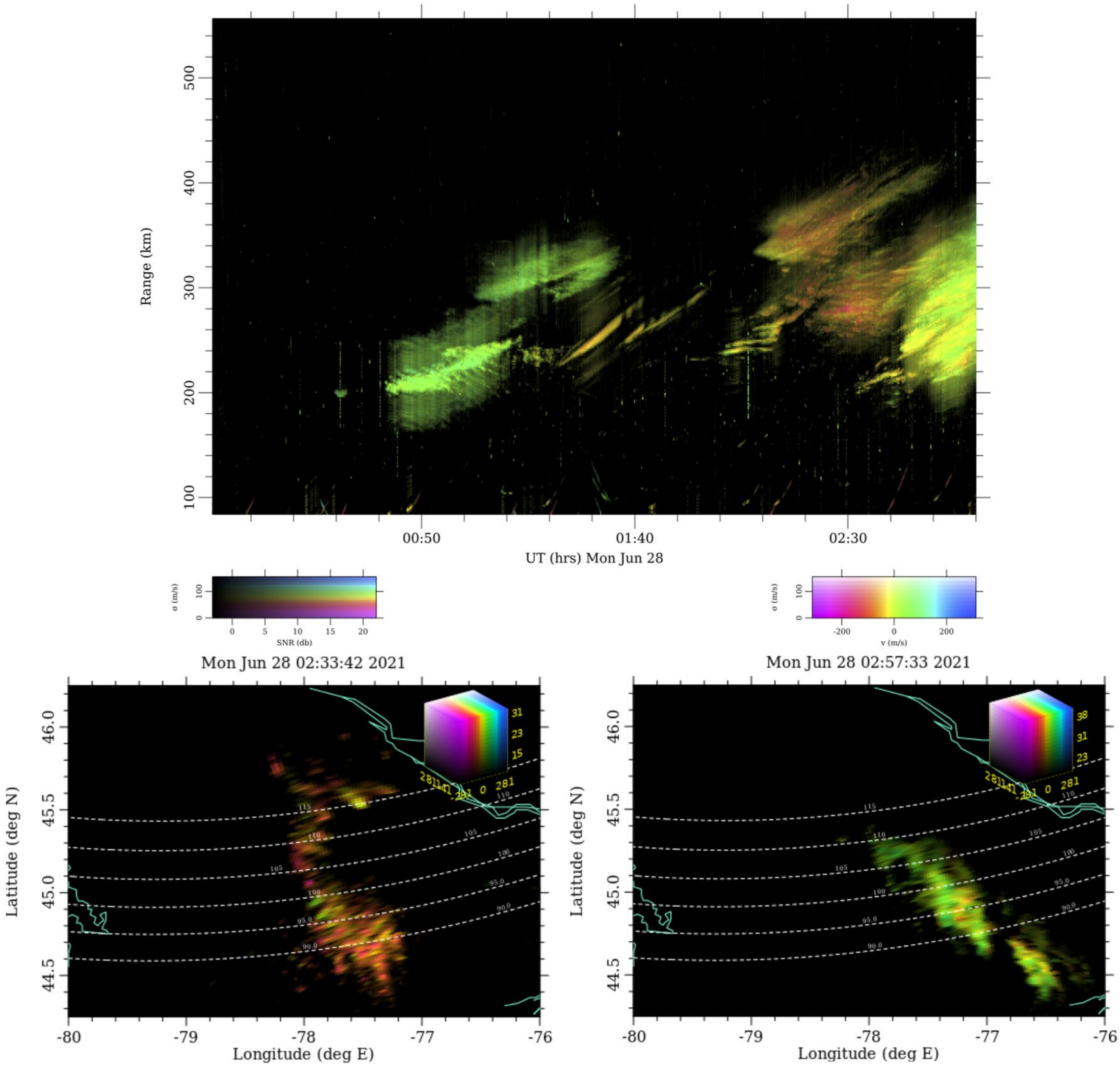

Figure 5. RTI plot (a) and radar images (b, c) for echoes observed on 28 June 2021, between 00:00 and 04:00 UT.

along with the Navier-Stokes equations:

$$u_t + uu_x + vu_y + wu_z + \frac{1}{R_o}p_x - \frac{2}{R_o}v = \frac{1}{R_e}(u_{xx} + u_{yy}) + \frac{1}{R_o}u_{zz} \tag{2}$$

$$v_t + uv_x + vv_y + wv_z + \frac{1}{R_o}p_y + \frac{2}{R_o}u = \frac{1}{R_e}(v_{xx} + v_{yy}) + \frac{1}{R_o}u_{zz} \tag{3}$$

$$w_t + uw_x + vw_y + ww_z + \frac{1}{R_o E_k}p_z = \frac{1}{R_e}(w_{xx} + w_{yy}) + \frac{1}{R_o}w_{zz} \tag{4}$$

Here, (u, v, w) are the zonal, meridional, and vertical wind components, p is the pressure, and subscripts (e.g., u_x, u_t) refer to derivatives in Cartesian space and time. The dimensionless parameters are the Ekman number E_k, Reynolds number R_e, and Rossby number R_o, defined below. In addition, we include a continuity equation for a passive tracer S obeying a standard convection-diffusion equation:

$$S_t + uS_x + vS_y + wS_z = \frac{1}{R_e}(S_{xx} + S_{yy} + S_{zz}) \tag{5}$$

For the purposes of this preliminary analysis, the tracer is a proxy for the unmagnetized E-region ions. The electrons, meanwhile, follow the ions to preserve quasineutrality. This is an admittedly elementary and oversimplified

10.1029/2022JA030929

treatment of plasma dynamics which neglects, among other phenomena, plasma instabilities which may be expected to contribute additional structuring. (A self-consistent treatment of coupled plasma/neutral dynamics is underway and the subject of follow-on work. The purpose of this analysis is merely to examine aspects of neutral dynamics in turning shears which should be present in the MLT but which are widely neglected.)

The model equations above have been non-dimensionalized through the following transformations (see e.g., Allen & Bridges, 2003):

$$x = \frac{x^*}{L}; \quad y = \frac{y^*}{L}; \quad z = \frac{z^*}{L\sqrt{E_k}}; \quad t = \frac{t^*U}{L} \tag{6}$$

$$u = \frac{u^*}{U}; \quad v = \frac{v^*}{U}; \quad w = \frac{w^*}{U\sqrt{E_k}}; \quad p = \frac{p^*}{\rho\Omega LU_f} \tag{7}$$

Here, the (*) superscript refers to dimensional quantities, U is a characteristic speed, L a characteristic length, and t is time. Also, ρ and p are density and pressure, respectively, and Ω is the effective angular rotation frequency (rotation frequency times sine of latitude).

The remaining dimensionless parameters of the equation are the Ekman number E_k, Reynolds number R_e, and Rossby number R_o, which are mutually related. In this definition, ν represents the kinematic viscosity. For the purposes of our illustrative simulations, the dimensionless parameters are treated as being invariant with altitude.

$$R_e = \frac{UL}{\nu}; \quad R_o = \frac{U}{\Omega L}; \quad E_k = \frac{R_o}{R_e} \tag{8}$$

It is well known that an equilibrium solution for this system of equations, subject to a non-slip condition at the lower boundary, exists and has the form of an Ekman spiral (e.g., Allen & Bridges, 2003):

$$u(x,y,z,t) = \cos(\alpha) - e^{-z}\cos(z-\alpha) \tag{9}$$

$$v(x,y,z,t) = \sin(\alpha) + e^{-z}\sin(z-\alpha) \tag{10}$$

$$w(x,y,z,t) = 0 \tag{11}$$

$$p(x,y,z,t) = p_\circ + 2x\sin(\alpha) - 2y\cos(\alpha) \tag{12}$$

$$S(x,y,z,t) = e^{-z/a} \tag{13}$$

where the α parameter sets the direction of the asymptotic (geostrophic) wind (the horizontal wind at $z \gg L$). As discussed above, this is an unstable equilibrium, and instability depends on the values of the Reynolds and Rossby numbers and, to some extent, on α.

4.2. Numerical Results

The numerical simulation is carried out using the Dedalus package (Burns et al., 2020). We use spectral gridding with a Chebychev basis in the vertical and Fourier bases in the horizontal, where the boundary conditions are periodic. Discretization is via a tau method. Time advance is by mixed implicit-explicit multistep integration obeying the CFL condition. Integration is carried forward in time 1,000 timesteps corresponding to 10,000 s or just over 2:45 hr of dimensional time.

For the simulations that follow, we take $L = 1$ km and $U = 100$ m/s. The kinematic viscosity in the MLT region is of the order 100–1,000 (Y. Yu et al., 2009), and so the non-dimensional Reynolds number should be in the range 100–1,000 as well. We furthermore take E_k to be unity in the subsequent analysis. We consider a box size $40 \times 40 \times 6L$ high. The initial conditions for the simulation are made to correspond to the Ekman spiral. The boundary conditions at the top and bottom of the simulation are made to correspond to the Ekman spiral equation evaluated at $z = 0$ and $z = 6L$, respectively. We take $\alpha = 90°$, corresponding to a northward asymptotic wind at the top of the spiral.

The simulation was run for a broad range of Reynolds numbers. As expected, we observe slow type-2 (rapid type-1) instability growth for Reynolds numbers greater than about 55 (113). When type-1 instability occurs, it dominates type 2. We further observe the growth of secondary instabilities leading to turbulence and, ultimately, wave breaking for Reynolds numbers greater than about 300. Varying α, the Ekman number, and box size causes quantitative but not qualitative variations in the simulation results. The larger the Reynolds number, the faster the onset of secondary instabilities. Results for $R_e = 330$ are fairly representative and will be discussed here.

Figure 6 shows results of the numerical simulations at three different stages of evolution. The isodensity contours reflect the density of the passive tracer S which we regard as a proxy for the electron density. The upper panel of the figure shows conditions after 52 min. Here, very regular waves or rolls with the characteristics of type-1 instability dominate. The waves are nearly stationary and tilted counter-clockwise about 15° with respect to the northward asymptotic wind imposed in the simulation. The dominant wavelength is approximately 10 km. The roll orientation and characteristic spacings are consistent with the theoretical studies discussed earlier in the paper.

By 104 min (middle panel), the wave forms become more irregular as waves due to type-2 instability begin to play a role. These waves are more slowly growing and have longer wavelengths than those due to type-1 instability, as described earlier, and they have a different alignment with respect to the asymptotic wind direction. They also propagate more rapidly. The superposition of the waves causes beating, with the resulting structure being somewhat irregular and exhibiting apparent phase propagation to the north.

Secondary waves begin to develop sometime after type-2 instability becomes apparent. The bottom panel shows conditions at 156 min by which time secondary waves are clearly visible. The secondary waves propagate to the north in a direction that is approximately normal to the primary waves caused by type-1 instability. The secondary waves are irregular but exhibit meridional structure mainly at scale sizes of a few km.

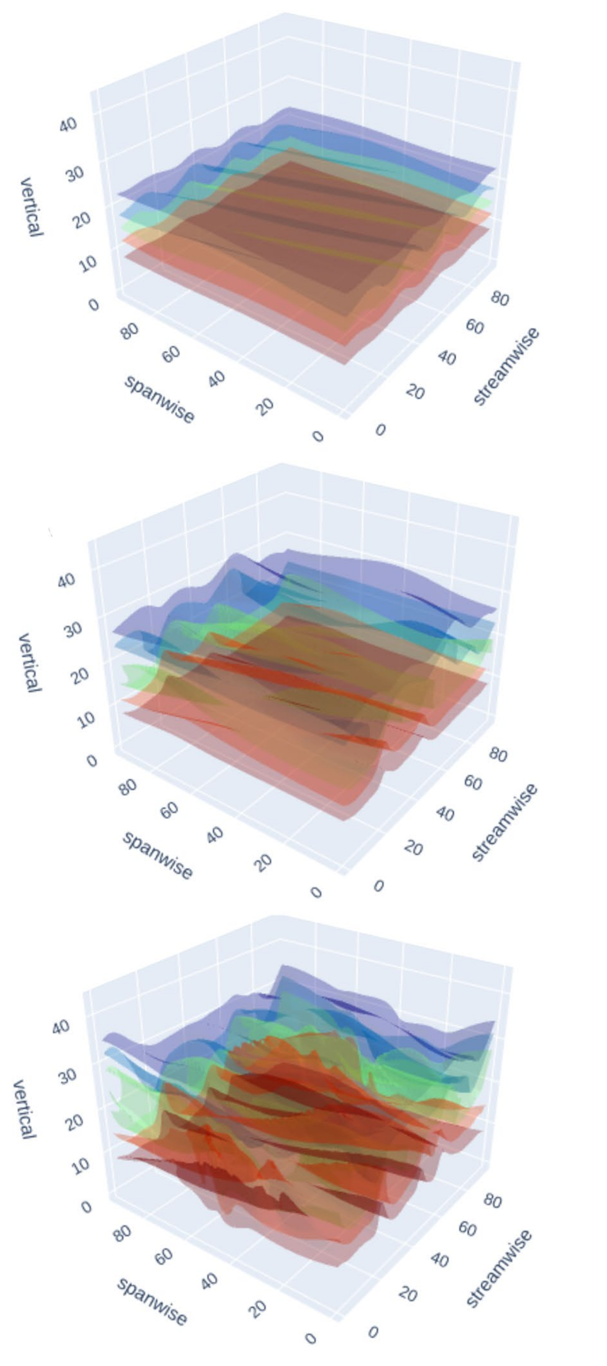

Figure 6. Ekman-type instability simulation results for $R_e = 330$. The isodensity surfaces are for the passive scalar S. (a) Flow 52 min after initialization, (b) Flow 104 min after initialization. (c) Flow 156 min after initialization. At first, the flow appears to be dominated by rapidly-growing, slowly-propagating type-1 waves elongated in the spanwise direction. Later, slow-growing, rapidly-propagating waves emerge and distort the flow. Finally, secondary instability sets in, leading to fine structure in the spanwise direction. The actual behavior observed depends on the Reynolds number (see text).

5. Analysis

The numerical simulations are initially dominated by type-1 instability, a turning-point instability characterized by nearly monochromatic plane waves. The waves are nearly stationary and have a wavelength of 10 L or 10 km in these simulations. The waves are qualitatively similar to the regular bands in the E_s-layer observations which also propagate slowly and exhibit wavelengths typically between 10 and 20 km. The association between primary E_s layer structuring and turning-point instability is a generalization of early work associating it with Kelvin Helmholtz instability.

In the simulation, the regular bands generated by type-1 instability are eventually joined by the effects of type-2 instability. The traveling waves resulting from type-2 instability have longer wavelengths and propagate at somewhat different directions compared to type-1 instability, and while the latter continue to dominate the simulations, the former cause a beating effect, leading to distortion. This distortion seems to be evident in the E_s-layer imagery which often shows primary banding which is spatially interrupted and bent.

The simulations presented here ultimately exhibit secondary instability. As the simulation does not include the effects of buoyancy, secondary instability is convective type. Secondary instability produces irregularities oriented approximately normally to the primary wavefronts with wavelengths approximately four time smaller. The secondary waves propagate in the direction parallel to the primary waves. The secondary waves appear to provide an explanation for the fine structure, cross-hatching or braiding, seen in the E_s-layer imagery. The fine structure

10.1029/2022JA030929

in the layers is also oriented approximately normal to the primary irregularity bands, exhibits wavelengths of a few km, and propagates along the wave fronts of the primary bands. The only large Doppler shifts within the radar observations are those associated with the secondary fine structure.

In the simulation, primary type-1 instability became clearly evident after about 30–45 min. Secondary instability, meanwhile, appeared after approximately 2 hr, and wave breaking was evident by the end of the simulation about 45 min later. These timescales depend on the characteristic flow speed U and especially on the Reynolds number R_e which can be highly variable in the MLT region. Consecutive QP echo events meanwhile occur quasi-periodically with a period of 30–90 min. The overlap is sufficiently close to suggest that the echo quasi-periodicity is related to the time it takes for neutral instability to form, grow, and break up.

Finally, whether type 1 primary instability or secondary instability occurs at all depends on whether the Reynolds number R_e exceeds a threshold value of approximately 110 and 300, respectively. As shown by Y. Yu et al. (2009), the Reynolds number varies steeply with altitude in the MLT region. As the altitude of E_s layers is also highly variable, and as radar echoes can only be observed at altitudes with E_s layers, we expect considerable day-to-day variability in QP echo occurrence. Whether and what kind of QP echoes are observed depends not only on whether E_s layers are present but also on the Reynolds number at the layer altitude. This may explain why some E_s layers are unstructured (blanketing), some exhibit primary irregularity bands, and some exhibit primary bands with fine structure (braiding).

6. Summary and Conclusions

The previous study from Hysell and Larsen (2021) using the same VHF imaging radar connected observations of sporadic- E in 2020 to Kelvin-Helmholtz instabilities. These radar images showed banded sporadic- E with traverse braided structuring that appeared to be indicative secondary instabilities caused by planar shearing of the Kelvin-Helmholtz type. The current study, based on observations in 2021, revealed the emergence of disorganized secondary banding, which we propose may be connected to secondary instabilities caused by turning shears of the Ekman type (Dubos et al., 2007).

The convective rolls that occur in turning shear represent a different type of instability than the smaller-scale Kelvin-Helmholtz shear instability that has been studied more extensively in the MLT region. The rolls can be long-lived and have a large along-axis extent. They also have a larger vertical extent. The characteristics of the rolls are discussed in more detail in the articles by Larsen et al. (2004) and Hurd et al. (2009) and are shown in the simulation results presented here. The larger static stability in the mesopause and lower thermosphere can act as a barrier to vertical transport. The upwelling and overturning associated with the instabilities not only drives the generation of plasma irregularity structure but also facilitates vertical transport in a region where vertical transport may otherwise be inhibited.

The plasma in the lower thermosphere is highly collisional, and the radar echo structures therefore give an indication of the behavior of the neutrals in the altitude range where the echoes occur. Observations of backscatter compared to neutral dynamical simulations generally appear to resemble similar morphology and overlapping quasi-periodicity. Nonetheless, there is only backscatter from regions where irregularities are present so that echo structures are one step removed from a direct observation of the neutral dynamics. Generation of irregularities is expected to be favored for neutral instabilities that have the preferred orientation for the echo bands, and this relationship thus acts a filter on the neutral instabilities that affect the radar echoes. We know from these observations that certain orientations are more favorable for producing the irregularity bands, specifically features propagating northeast to southwest. The relationship between neutral instability orientation and the generation of observable irregularity echoes needs to be investigated further. Presumably this is best done through more sophisticated modeling than what was presented here. Future work will include an expansion of the current simulation to add equations describing plasma dynamics and neutral-ion collisions.

Data Availability Statement

Data discussed in this paper can be accessed through the Cornell eCommons repository through https://doi.org/10.7298/8sxf-b977.2. Numerical simulations were generated using Dedalus, an open-source spectral solver available at https://dedalus-project.org (Burns et al., 2020).

Acknowledgments

The work was supported by NSF awards AGS-2011304 to Cornell University and AGS-2012994 to Clemson University.

References

Allen, L., & Bridges, T. (2003). Hydrodynamic stability of the Ekman boundary layer including interaction with complaint surface: A numerical framework. *European Journal of Mechanics - B: Fluids*, *22*(3), 239–258. https://doi.org/10.1016/s0997-7546(03)00036-0

Burns, K. J., Vasil, G. M., Oishi, J. S., Lecoanet, D., & Brown, B. P. (2020). Dedalus: A flexible framework for numerical simulations with spectral methods. *Physical Review Research*, *2*, 023068. https://doi.org/10.1103/PhysRevResearch.2.023068

Chu, Y. H., & Wang, C. Y. (1997). Interferometry observations of 3-dimensional spatial structures of sporadic *E* using the Chung-Li VHF radar. *Radio Science*, *32*(2), 817–832. https://doi.org/10.1029/96rs03578

Coleman, G., Ferziger, J., & Spalart, P. (1990). A numerical study of the turbulent Ekman layer. *Journal of Fluid Mechanics*, *213*(1), 742–757. https://doi.org/10.1017/s0022112090002348

Cosgrove, R. B., & Tsunoda, R. T. (2002). A direction-dependent instability of sporadic- *E* layers in the nighttime midlatitude ionosphere. *Geophysical Research Letters*, *29*(18), 11-1–11-14. https://doi.org/10.1029/2002JA009728

Cosgrove, R. B., & Tsunoda, R. T. (2004). Instability of the *E*–*F* coupled nighttime midlatitude ionosphere. *Journal of Geophysical Research*, *109*(A4), A04305. https://doi.org/10.1029/2003JA010243

Dubos, T., Barthlott, C., & Drobinski, P. (2007). Emergence of secondary instability of Ekman layer rolls. *Journal of the Atmospheric Sciences*, *65*(7), 2326–2342. https://doi.org/10.1175/2007jas2550.1

Ekman, V. W. (1905). On the influence of the earth's rotation on ocean currents. *Ark. Math. Astronoi Fys.*, *2*(11), 53.

Faller, A., & Kaylor, R. (1966). A numerical study of the instability of the laminar Ekman boundary layer. *Journal of the Atmospheric Sciences*, *23*(5), 466–480. https://doi.org/10.1175/1520-0469(1966)023<0466:ansoti>2.0.co;2

Fukao, S., Yamamoto, M., Tsunoda, R. T., Hayakawa, H., & Mukai, T. (1998). The SEEK (sporadic- *E* experiment over Kyushu) campaign. *Geophysical Research Letters*, *25*(11), 1761–1764. https://doi.org/10.1029/98gl00932

Hecht, J. H., Liu, A. Z., Bishop, R. L., Clemmons, J. H., Gardner, C. S., Larsen, M. F., & Walterscheid, R. L. (2004). An overview of observations of unstable layers during the Turbulent Oxygen Mixing Experiments (TOMEX). *Journal of Geophysical Research*, *109*(D2), D02S01. https://doi.org/10.1029/2002JD003123

Hurd, L., Larsen, M. F., & Liu, A. Z. (2009). Overturning instability in the mesosphere and lower thermosphere: Analysis of instability conditions in lidar data. *Annales Geophysicae*, *27*(7), 2937–2945. https://doi.org/10.5194/angeo-27-2937-2009

Hysell, D. L., & Burcham, J. (1999). HF radar observations of quasiperiodic *E* layer echoes over North America. *Journal of Geophysical Research*, *104*(A3), 4361–4371. https://doi.org/10.1029/1998ja900144

Hysell, D. L., & Chau, J. L. (2006). Optimal aperture synthesis radar imaging. *Radio Science*, *41*(2), RS2003. https://doi.org/10.1029/2005RS003383

Hysell, D. L., & Larsen, M. F. (2021). VHF imaging radar observations and theory of banded midlatitude sporadic *E* ionization layers. *J. Geophys. Res. Space Phys.*, *126*(5), e2021JA029257. https://doi.org/10.1029/2021JA029257

Hysell, D. L., Larsen, M. F., Fritts, D. C., Laughman, B., & Sulzer, M. P. (2018). Major upwelling and overturning in the mid-latitude F region ionosphere. *Nature Communications*, *9*(3326), 3326. https://doi.org/10.1038/s41467-018-05809-x

Hysell, D. L., Nossa, E., Larsen, M. F., Munro, J., Smith, S., Sulzer, M. P., & González, S. A. (2012). Dynamic instability in the lower thermosphere inferred from irregular sporadic layers. *Journal of Geophysical Research*, *117*, A8. https://doi.org/10.1029/2012JA017910

Hysell, D. L., Yamamoto, M., & Fukao, S. (2002a). Imaging radar observations and theory of type I and type II quasi-periodic echoes. *Journal of Geophysical Research*, *107*(A11), 1360. https://doi.org/10.1029/2002ja009292

Hysell, D. L., Yamamoto, M., & Fukao, S. (2002b). Simulations of plasma clouds in the midlatitude *E* region ionosphere with implications for type I and type II quasiperiodic echoes. *Journal of Geophysical Research*, *107*(A10), 1313. https://doi.org/10.1029/2002ja009291

Jaynes, E. T. (1982). On the rationale of maximum-entropy methods. *Proceedings of the IEEE*, *70*(9), 939–952. https://doi.org/10.1109/proc.1982.12425

Larsen, M. F. (2000). A shear instability seeding mechanism for quasi-periodic radar echoes. *Journal of Geophysical Research*, *105*(A11), 24931–24940. https://doi.org/10.1029/1999ja000290

Larsen, M. F., Fukao, S., Yamamoto, M., Tsunoda, R., Igarashi, K., & Ono, T. (1998). The SEEK chemical release experiment: Observed neutral wind profile in a region of sporadic- *E*. *Geophysical Research Letters*, *25*(11), 1789–1792. https://doi.org/10.1029/98gl00986

Larsen, M. F., Hysell, D. L., Zhou, Q. H., Smith, S. M., Friedman, J., & Bishop, R. L. (2007). Imaging coherent scatter radar, incoherent scatter radar, and optical observations of quasiperiodic structures associated with sporadic *E* layers. *Journal of Geophysical Research*, *112*(A6), A06321. https://doi.org/10.1029/2006JA012051

Larsen, M. F., Liu, A. Z., Gardner, C. S., Kelley, M. C., Collins, S., Friedman, J., & Hecht, J. H. (2004). Observations of overturning in the upper mesosphere and lower thermosphere. *Journal of Geophysical Research*, *109*(D2), D02S04. https://doi.org/10.1029/2002JD003067

Layzer, D. (1969). New theory of mid-latitude sporadic E. *Nature*, *223*(5208), 794–797. https://doi.org/10.1038/223794a0

Leibovich, S., & Lele, S. (1985). The influence of the horizontal component of the earth's angular velocity on the instability of the Ekman layer. *Journal of Fluid Mechanics*, *150*, 41–87. https://doi.org/10.1017/s0022112085000039

Lilly, D. (1966). On the instability of Ekman boundary flows. *Journal of the Atmospheric Sciences*, *23*(5), 481–494. https://doi.org/10.1175/1520-0469(1966)023<0481:otioeb>2.0.co;2

Lingwood, R. J. (1995). Absolute instability pf the boundary layer on a rotating disk. *Journal of Fluid Mechanics*, *299*, 17–33. https://doi.org/10.1017/s0022112095003405

Liu, H.-L. (2017). Large wind shears and their implications for diffusion in regions with enhanced static stability: The mesopause and the tropopause. *Journal of Geophysical Research: Atmospheres*, *122*(18), 9579–9590. https://doi.org/10.1029/2002jd003067

Mason, P., & Sykes, R. (1980). A two-dimensional numerical study of horizontal roll vortices in the neutral atmospheric boundary layer. *Quarterly Journal of the Royal Meteorological Society*, *106*(448), 351–366. https://doi.org/10.1002/qj.49710644808

Miller, K. L., & Smith, L. G. (1978). Incoherent scatter radar observations of irregular structure in mid-latitude sporadic *E* layers. *Journal of Geophysical Research*, *83*(A8), 3761. https://doi.org/10.1029/ja083ia08p03761

Rao, N. V., Patra, A. K., & Rao, S. V. B. (2008). Some new aspects of low-latitude *E*-region QP echoes revealed by Gadanki radar: Are they due to Kelvin-Helmholtz instability or gravity waves? *Journal of Geophysical Research*, *113*, A03309. https://doi.org/10.1029/2007JA012574

Riggin, D., Swartz, W. E., Providakes, J., & Farley, D. T. (1986). Radar studies of long-wavelength waves associated with mid-latitude sporadic *E* layers. *Journal of Geophysical Research*, *91*(A7), 8011. https://doi.org/10.1029/ja091ia07p08011

Seyler, C. E., Rosado-Roman, J. M., & Farley, D. T. (2004). A nonlocal theory of the gradient-drift instability in ionospheric plasmas at midlatitudes. *Journal of Atmospheric and Solar-Terrestrial Physics*, *66*(17), 1627–1637. https://doi.org/10.1016/j.jastp.2004.07.011

Skilling, J., & Bryan, R. K. (1984). Maximum entropy image reconstruction: General algorithm. *Monthly Notices of the Royal Astronomical Society*, *211*(1), 111–124. https://doi.org/10.1093/mnras/211.1.111

10.1029/2022JA030929

Smith, L. G., & Miller, K. L. (1980). Sporadic- *E* layers and unstable wind shears. *Journal of Atmospheric and Terrestrial Physics*, *42*(1), 45–50. https://doi.org/10.1016/0021-9169(80)90122-1

Swartz, W. E., Kelley, M. C., Makela, J. J., Collins, S. C., Kudeki, E., Franke, S., et al. (2000). Coherent and incoherent scatter radar observations during intense mid-latitude spread *F*. *Geophysical Research Letters*, *27*(18), 2829–2832. https://doi.org/10.1029/2000gl000021

Thompson, A. R. (1986). Interferometry and synthesis in radio astronomy

Whitehead, J. D. (1972). The structure of sporadic *E* from a radio experiment. *Radio Science*, *7*(3), 355–358. https://doi.org/10.1029/rs007i003p00355

Whitehead, J. D. (1989). Recent work on mid-latitude and equatorial sporadic *E*. *Journal of Atmospheric and Terrestrial Physics*, *51*(5), 401–424. https://doi.org/10.1016/0021-9169(89)90122-0

Woodman, R. F., Chau, J. L., Aquino, F., Rodriguez, R. R., & Flores, L. A. (1999). Low-latitude field-aligned irregularities observed in the *E* region with the Piura VHF radar: First results. *Radio Science*, *34*(4), 983–990. https://doi.org/10.1029/1999rs900027

Yamamoto, M., Fukao, S., Ogawa, T., Tsuda, T., & Kato, S. (1992). A morphological study of mid-latitude *E*-region field-aligned irregularities observed with the MU radar. *Journal of Atmospheric and Solar-Terrestrial Physics*, *54*(6), 769–777. https://doi.org/10.1016/0021-9169(92)90115-2

Yamamoto, M., Fukao, S., Woodman, R. F., Ogawa, T., Tsuda, T., & Kato, K. (1991). Mid-latitude *E* region field-aligned irregularities observed with the MU radar. *Journal of Geophysical Research*, *96*(15), 943–15949. https://doi.org/10.1029/91ja01321

Yu, T. Y., Palmer, R. D., & Hysell, D. L. (2000). A simulation study of coherent radar imaging. *Radio Science*, *35*(5), 1129–1141. https://doi.org/10.1029/1999rs002236

Yu, Y., Hickey, M. P., & Liu, Y. (2009). A numerical model characterizing internal gravity wave propagation into the upper atmosphere. *Advances in Space Research*, *44*(7), 836–846. https://doi.org/10.1016/j.asr.2009.05.014